# Comparison of electron-beam-melted and conventionally rolled Inconel 718 under thermomechanical creep-fatigue loading

Stefan Guth [a,*], Tomaš Babinský [b,c] , Steffen Antusch [a], Alexander Klein [a], Daniel Kuntz [a], Ivo Šulák [b]

[a] *Institute for Applied Materials, Karlsruhe Institute of Technology, Engelbert-Arnold-Strasse 4, D-76128 Karlsruhe, Germany*
[b] *Institute of Physics of Materials ASCR, Žižkova 22, 616 00 Brno, Czech Republic*
[c] *Paul Scherrer Institut, PSI, Forschungsstrasse 111, 5232 Villigen PSI, Switzerland*

## ARTICLE INFO

## ABSTRACT

To evaluate the potential of additively manufactured superalloys for high-temperature components, strain-controlled thermomechanical fatigue tests were performed on the Ni-based superalloy Inconel 718 in conventional and electron-beam-melted (EBM) form. While EBM specimens feature columnar grains with strong [001]-texture along the building direction, conventional specimens exhibit equiaxed polygonal grains without pronounced texture. All tests ran under in-phase conditions with a temperature range of 300–650 °C. In some tests, 10 min dwell times at 650 °C at the peak tensile strain were added to induce severe creep-fatigue interaction. For a given mechanical strain amplitude, the lifetimes of EBM specimens exceed those of conventional ones. This is mainly caused by the lower elastic modulus of the EBM specimens due to their strong [001]-texture resulting in lower cyclic stress amplitudes. Typical for creep-fatigue loading, the damage is mainly intergranular. The EBM material cracks predominantly at boundaries of fine equiaxed grains, while the conventional material suffers also from twin boundary cracking. Electron microscopy characterisation reveals that the strengthening γ' and γ'' precipitates develop differently in conventional and EBM specimens during thermomechanical cycling, which affects their deformation and lifetime behaviour. The findings suggest that EBM-manufactured superalloys can be a beneficial alternative for hot-operating components.

## 1. Introduction

Inconel 718 is a Nickel-based superalloy widely used as a structural material for high-temperature components due to its excellent strength and resistance to creep, corrosion, and fatigue at elevated temperatures. The outstanding high-temperature strength is based on finely dispersed precipitates of the γ'' phase ($Ni_3Nb$) and, to a lesser extent, the γ' phase ($Ni_3(Al,Ti)$), which are coherent with the fcc γ matrix and effectively impede dislocation motion. At temperatures above 700 °C, the meta-stable γ'' precipitates may transform into the incoherent δ phase, which has the same $Ni_3Nb$ composition [1]. This transformation results in a significant decrease in tensile and yield strength above 650 °C [2].

Conventional processing routes for Inconel 718 are forging, casting and powder metallurgy. However, due to its excellent weldability, it is also one of the most commonly employed materials for metal additive manufacturing (AM) [3]. For components made of Inconel 718, AM methods offer not only unparalleled design freedom but also allow

generating specific microstructures that are difficult or even impossible to achieve by conventional manufacturing [4,5].

In high-temperature components, the materials suffer from thermomechanical fatigue (TMF), which arises from thermal strain gradients due to start-up, load change and shutdown operations. In many cases, crack initiation and growth due to TMF determine the lifetime of these components. Depending on the considered volume element subjected to TMF, the phase angle between temperature and mechanical strain varies. In laboratory studies, two extreme cases of phase relations, namely in-phase (IP, phase angle of 0°) and out-of-phase (OP, phase angle of 180°), are typically considered. Under IP TMF loading, high temperatures coincide with tensile stresses, resulting in severe creep-fatigue interaction. For polycrystalline alloys, this may induce cavities on grain boundaries [6] or cracks on grain boundary triple points due to grain boundary sliding [7]. Due to this grain boundary degradation, IP TMF damage in polycrystalline alloys is often vastly intergranular [7–10]. Selective grain boundary oxidation may further contribute to

---

\* Corresponding author.
*E-mail address:* stefan.guth@kit.edu (S. Guth).

intergranular cracking [9], however, IP TMF tests in vacuum have shown that oxidation is not necessary to produce predominantly intergranular damage [8]. In order to simulate steady state service at elevated temperatures, additional tensile dwell times at maximum temperature can be introduced to an IP TMF cycle. In that case, the amount of intergranular damage typically increases [11] and lifetimes reduce [12,13]. The isothermal fatigue behaviour of conventionally manufactured Inconel 718 has been extensively investigated [12,14–18]. However, for TMF loading on smooth specimens, there is rather few data available. An early work from Kuwabara et al. showed that for temperature cycling between 300 and 650 °C, lifetimes under IP conditions are shorter than under OP conditions [19]. Later, Sun et al. and Deng et al. confirmed this behaviour for temperature ranges of 300–650 °C [20] and 350–650 °C [10], respectively. Both studies also found that IP TMF lifetimes are shorter than those of isothermal low cycle fatigue at the maximum temperature of the TMF cycle [10,20]. Thus, for Inconel 718 components subject to IP TMF, design based on isothermal fatigue data may be non-conservative, emphasizing the need for TMF data. Conversely, Evans et al. reported OP-TMF to be most critical for a temperature range of 300–680 °C indicating a high sensitivity of lifetimes on the maximum temperature [21].

To reduce susceptibility to grain boundary damage caused by creep and creep-fatigue interaction, directionally solidified (DS) alloys with a columnar grain structure have been developed [22]. Under uniaxial loading, such alloys exhibit only few grain boundaries perpendicular to the loading direction, which is particularly beneficial under IP TMF loading where grain boundaries are prone to crack initiation and propagation. While DS alloys are typically cast, AM by electron beam melting (EBM) can produce similar columnar-grained microstructures with grains extending along the building direction. Such EBM microstructures may offer similar advantages under creep and creep-fatigue loading [4,5,23]. Under isothermal fatigue loading at 650 °C, Kirka et al. [24] have shown that columnar-grained EBM Inconel 718 is superior to conventional Inconel 718, when the loading axis is parallel to the EBM building direction. Likewise, Deng et al. [25] found that EBM Inconel 718 exhibits higher crack growth resistance than forged Inconel 718 under isothermal fatigue loading at 550 °C. A previous study by the authors indicated that the EBM Inconel 718 might outperform conventionally wrought Inconel 718 also under IP TMF loading [26]. With this follow-up study, we aim to validate this assumption by directly comparing the TMF IP behaviour of EBM and conventionally rolled Inconel 718. Therefore, we conducted strain-controlled IP TMF tests on conventionally rolled specimens under the same conditions as those used for the tests on EBM Inconel 718 reported in [26], specifically a temperature range of 300 °C to 650 °C with optional dwell times of 600 s at 650 °C. Special emphasis is placed on the evolution of microstructure and damage in order to gain a better understanding of how varying initial microstructures affect the TMF behaviour of Inconel 718.

## 2. Experimental

### 2.1. Material

The conventionally rolled Inconel 718 was supplied in the form of a round bar, which underwent a standard heat treatment including solution annealing at 1065 °C for two hours, followed by a two-stage ageing at 718 °C and at 621 °C for 8 h each and eventually cooling in air. The EBM raw specimens were manufactured in near net shape geometry using an Arcam A2X machine from Colibrium Additive (formerly GE Additive). The specimen loading axis (LA) was parallel to the building direction (BD). More details on the EBM specimen manufacturing process can be found in [26]. After manufacturing, the EBM raw specimens were hot isostatically pressed (HIP) for 4 h at 1120 °C and 100 MPa, followed by an identical heat treatment as the conventional specimens. Table 1 gives the chemical composition of both specimen types after manufacturing and heat treatments measured by optical emission

**Table 1**
Chemical composition of specimens in wt.%.

| | C | Cr | Mo | Nb | Ti | Al | Fe | Ni |
|---|---|---|---|---|---|---|---|---|
| **Conventional Inconel 718** | 0.03 | 18.3 | 2.8 | 4.7 | 0.86 | 0.52 | 18.4 | Bal. |
| **EBM-manufactured Inconel 718** | 0.04 | 18.3 | 2.9 | 4.5 | 0.89 | 0.56 | 18.8 | Bal. |

spectroscopy using a SpectroLab M10 device. For both manufacturing processes, all elements are within the specification [2] and the differences between the two manufacturing routes are marginal.

From both EBM raw specimens and the conventionally rolled bar, solid round fatigue-testing specimens with a cylindrical gauge length of 10 mm and a gauge length diameter of 4.3 mm were machined by turning. Using the Archimedes method with ethanol, the density of the EBM specimens was measured as $8190 \pm 15$ kg/m$^3$ [26], while the density of the conventional material was determined to be $8190 \pm 8$ kg/m$^3$. This indicates a high relative density of the EBM specimens of almost 100 %, which was anticipated as a result of the HIP treatment. SEM analyses of gauge length sections of EBM specimen revealed only infrequent pores of diameters below 50 μm. Consequently, we expect only a minor influence of processing defects on the TMF behaviour of the EBM specimens.

Fig. 1 presents EBSD and TEM pictures of conventional and EBM Inconel 718 in the initial state after the heat treatments. While the conventional material exhibits equiaxed polygonal grains with random orientation and many annealing twins, the EBM material consists mainly of grains elongated along the building direction and show a pronounced < 001 > texture. However, there are also clusters of fine equiaxed grains, which have also a varying orientation. No annealing twins could be found in the EBM material. The conventional material primarily exhibits fine disc-shaped γ'' precipitates and, more rarely, cube-shaped γ' precipitates – both typical for Inconel 718 [15,17,27]. The EBM material also primarily exhibits disc-shaped γ'' precipitates, along with a significant amount of cube-shaped γ' precipitates and larger disc-shaped δ precipitates. As reported in our previous study and also by Kirka et al., the EBM material exhibits cell structures with δ precipitates forming the cell boundaries [26,28]. The mean size (disc diameter) of the γ'' precipitates in the conventional material was measured as $52 \pm 3.7$ nm with an aspect ratio of approximately 0.6. In the EBM material, the mean γ'' precipitate size (disc diameter) was found to be $57.8 \pm 5$ nm with an aspect ratio of approximately 0.43. Hence, while the γ'' discs exhibit similar diameters in both materials, they are approximately 25 % thinner in the EBM material. In the EBM material, the disc-shaped δ phase precipitates exhibit a mean size (disc diameter) of $266.5 \pm 73.6$ nm, with an aspect ratio of approximately 0.17, while the cube-shaped γ' precipitates show a mean edge length of $76.2 \pm 13.7$ nm.

The elastic modulus of each specimen was measured prior to TMF testing from the unloading curve of a 3 kN load, which corresponds to about 200 MPa and is thus safely in the elastic regime. At room temperature, the measured mean values are $218.7 \pm 2.9$ GPa for conventional specimens and $144.9 \pm 3.6$ GPa for EBM specimens. At the mean temperature of the TMF cycle of 475 °C, the mean elastic modulus is $189.5 \pm 2.8$ GPa for conventional specimens and $121.8 \pm 3.0$ GPa for EBM specimens. The significantly lower elastic moduli of the EBM specimens originate from the observed < 001 > texture in combination with a low elastic modulus in the [001] direction for Ni-based alloys [29]. The initial Vickers hardness values of the specimens were measured as $494 \pm 28$ HV1 for conventional material and $453 \pm 15$ HV1 for EBM material using a QNess Q10 A + hardness tester.

### 2.2. Thermomechanical fatigue testing

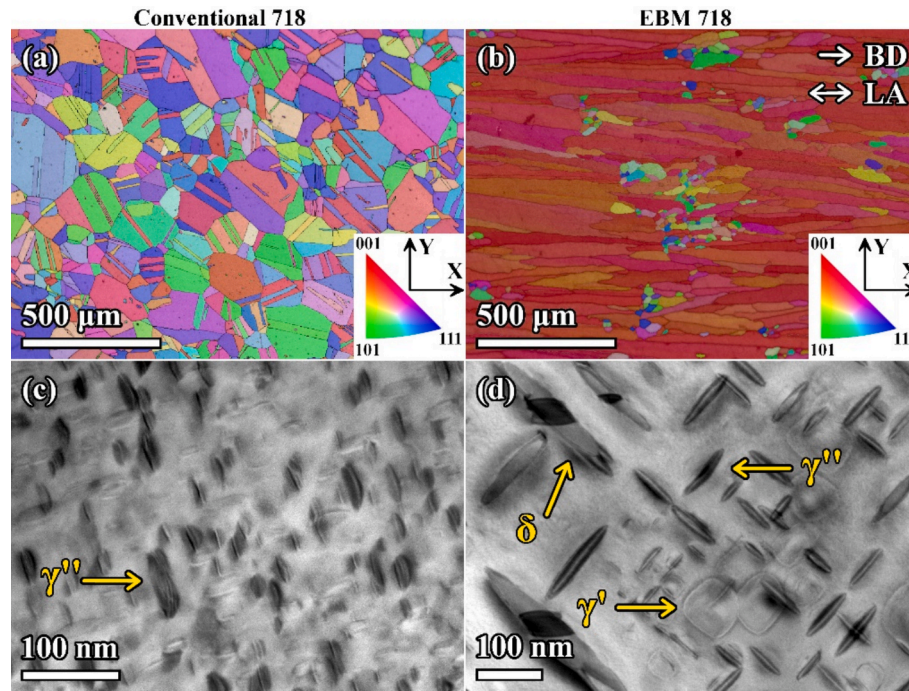The TMF tests were conducted in laboratory air under fully reversed

**Fig. 1.** Microstructure in the initial state. (a) EBSD image of conventional Inconel 718, (b) EBSD image of EBM Inconel 718, (c) TEM image of conventional Inconel 718, (d) TEM image of EBM Inconel 718.

($R_\varepsilon = -1$) axial strain control mode as described in [26]. A servo-electric Zwick testing machine with a load capacity of 100 kN was employed. Axial strain was measured and controlled using a capacitive extensometer with 10 mm initial length, which was mounted in the specimen gauge section using alumina rods. The specimens were heated inductively using a water-cooled copper coil and a 5 kW high frequency generator. Cooling was realized by thermal conduction into the water-cooled grips. The temperature was measured and controlled with ribbon-type thermocouples of type K (NiCr-Ni) wrapped around the gauge length centre. All tests were conducted under IP TMF conditions with a temperature range of 300–650 °C. The start of a cycle and thus the start of the first loading was at the mean temperature of 475 °C. For both materials, two TMF-cycle shapes were compared: 1) an equal ramp (ER)

cycle with triangular shape and 2) a dwell time (DT) cycle with additional 600 s dwell times at maximum temperature and maximum (tensile) strain. Fig. 2 shows a schematic of the ER and DT cycles. The heating and cooling rate was 5 K/s for both cycle types, resulting in a cycle time of 140 s for ER loading and of 740 s for DT loading. Prior to each test, the thermal strain corresponding to a cycle was measured by cycling the temperature at controlled zero force. The course of the controlling total strain for the load cycles was then calculated by adding the desired mechanical strain–time course to the measured thermal strain–time course ($\varepsilon_t = \varepsilon_{th} + \varepsilon_{mech}$). The tested mechanical strain amplitudes $\varepsilon_{a,mech}$ varied between 0.4 and 0.8 %, resulting in lifetimes between about 100 and 10,000 cycles. The TMF lifetime (number of cycles to failure, $N_f$) was determined using a 10 % drop of the stabilised
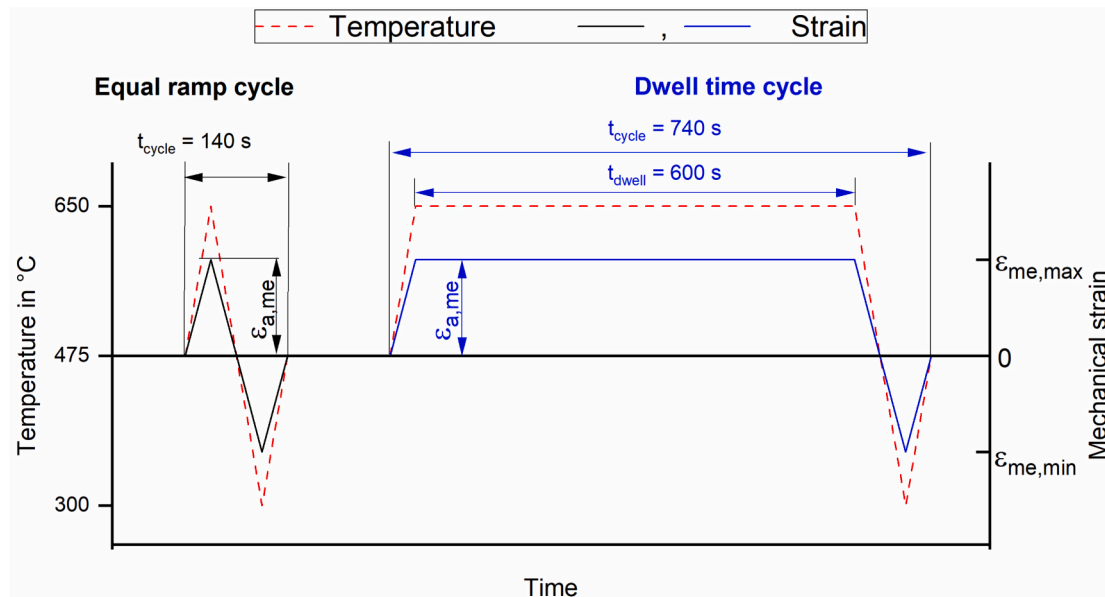


**Fig. 2.** Courses of temperature and mechanical strain in equal ramp (ER) and dwell time (DT) TMF cycling.

maximum stress as failure criterion.

## 2.3. Observations

The analysis of the initial microstructure was performed on sections prepared post-test from specimen grip sections. The maximum temperature in the grip section area during TMF cycling was measured by a thermocouple to be approximately 210 °C. Therefore, we assume that the specimen grip section of a tested specimen is representative of the initial microstructure. The grip sections were sectioned longitudinally (parallel with the load axis) and analysed for texture by electron back scatter diffraction (EBSD). A more detailed microstructural analysis was conducted on thin foils which were prepared from the longitudinal sections and observed in transmission electron microscope (TEM).

Fracture surfaces of fractured specimens and longitudinal sections of the gauge lengths were observed with scanning electron microscopy (SEM). The overall damage was observed in secondary electron contrast (SE) and with EBSD technique. Further post-test characterization of deformation structures was conducted by electron channelling contrast imaging (ECCI) and finally by TEM.

Sections observed in SEM were ground with SiC paper to a grit size of P1200, and treated in electrolytical polisher Struers LectroPol-5 using an electrolyte consisting of 93.9 vol% ethanol, 1.4 vol% nitric acid and 4.7 vol.% perchloric acid at −15 °C/54 V/6–10 s. TEM foils were prepared using a standard procedure involving electrolytical thinning. Approximately 3-mm-wide plates (cut off parallel to the load axis) were ground down to 70 μm, and thinned electrolytically in a double jet device Struers TenuPol2 using an electrolyte consisting of 70 vol% methanol, 20 vol% glycerine and 10 vol.% perchloric acid at −5 °C/11 V/ca. 40 mA/90–120 s until the foil was sufficiently thin for TEM observation (~100 nm).

Microstructural observations were conducted using the following instruments. SEM system Tescan LYRA 3 XMU FEG/SEMxFIB equipped with a YAG SE detector, retractable annular YAG scintillator type back scatter electron (BSE) detector allowing ECCI observations, and electron back scatter diffraction (EBSD) detector Symmetry 2 by Oxford Instruments. Transmission Kikuchi diffraction (TKD) was conducted on TEM foils in the SEM. The SEM was operated at 10 kV (SE, BSE), 20 kV (EBSD, ECCI) and 30 kV (TKD). More detailed observations were performed using a TEM system JEOL JEM-2100-F with direct beam (diffraction pattern analyses) and convergent beam (scanning TEM; STEM) in bright field (BF) mode. The TEM was operated at 200 kV. Precipitate sizes based on TEM micrographs were measured with the program VGSTUDIO MAX by Hexagon.

## 3. Results

### 3.1. TMF lifetime

Fig. 3 shows the lifetime results dependent on the mechanical strain amplitude (left) and on the stress amplitude at half of the lifetime (right). For a given mechanical strain amplitude (Fig. 3a), EBM specimens show generally longer lifetimes than conventional specimens. Introducing dwell times reduces the lifetimes of conventional specimens. This trend increases with increasing strain amplitudes. For EBM specimens, introducing dwell times reduces the lifetime for lower strain amplitudes and prolongs lifetimes for higher strain amplitudes. Consequently, the EBM Inconel 718 outperforms conventional Inconel 718, particularly under dwell time loading at higher strain amplitudes. When the stress amplitude at half of the lifetime is considered a loading variable (Fig. 3b), both EBM and conventional lifetimes fall roughly into a common scatter band. A more detailed examination shows that for ER cycling, the lifetimes at a given stress amplitude are slightly longer for the conventional specimens than for the EBM specimens. For DT cycling, the stress amplitudes at half of the lifetime for EBM and conventional specimens do not overlap; therefore, a direct comparison of lifetimes at a given stress amplitude is not possible. However, it appears that also for DT cycling, conventional specimens show slightly longer lifetimes at a given stress amplitude. In this representation, introducing dwell times has only a negligible influence on the resulting lifetime for both EBM and conventional specimens.

### 3.2. Cyclic deformation behaviour

Fig. 4 compares the stress–strain hysteresis loops at half of the lifetime for conventional and EBM material in ER (Fig. 4a) and DT (Fig. 4b) cycles, at a representative strain amplitude of 0.6 %. Typically for IP TMF testing, the stresses induced at high temperatures are lower than those induced at lower temperatures leading to a negative mean stress. It can be seen that, for the DT cycle, the stress relaxes at constant maximum strain during the dwell periods. For both cycle types, the slope in the elastic regimes reflecting the elastic modulus is significantly higher for the conventional material. This results in higher stress amplitudes for the conventional material than for the EBM material at a given total strain amplitude. The plastic strain amplitude is also considerably higher for conventional material, particularly under ER cycling. While for conventional material, introducing dwell times leads to an increased yield stress and thus a higher stress amplitude at half of the lifetime, the opposite is true for EBM material.

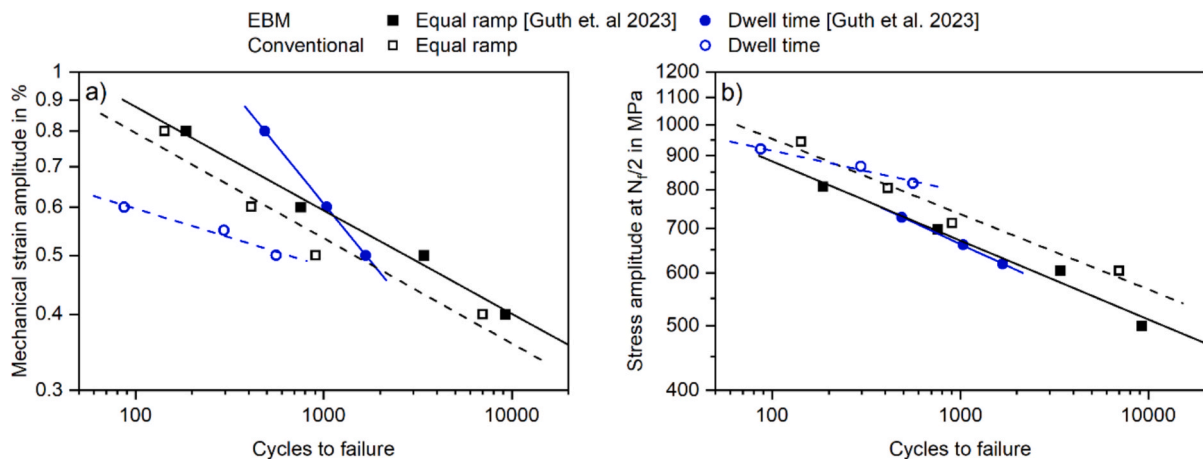Fig. 5 shows the relationship between stress amplitude and plastic



**Fig. 3.** Comparison of TMF lifetimes of conventional and EBM Inconel 718 in mechanical strain amplitude-life representation (a) and stress amplitude-life representation (b). The results for EBM material have been already reported in Guth et. al 2023 [26].
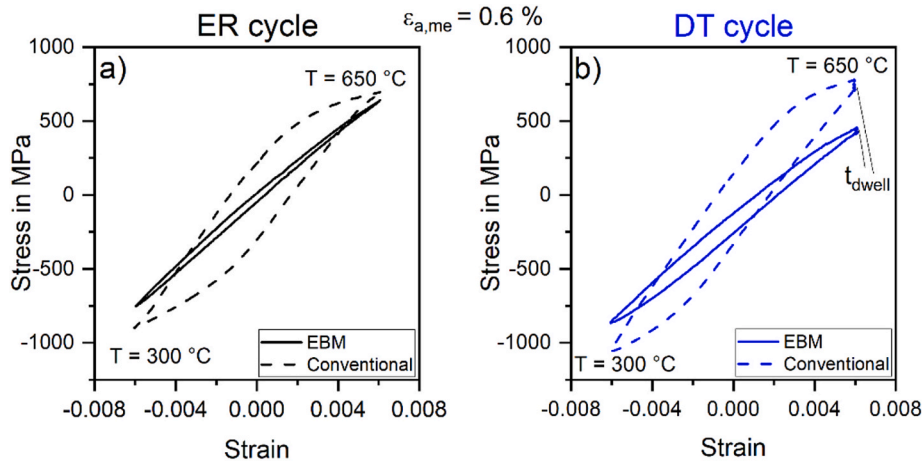
**Fig. 4.** Influence of manufacturing method on the stress–strain hysteresis loops at half of the lifetime for a mechanical strain amplitude of 0.6 %. a) ER cycle, b) DT cycle.
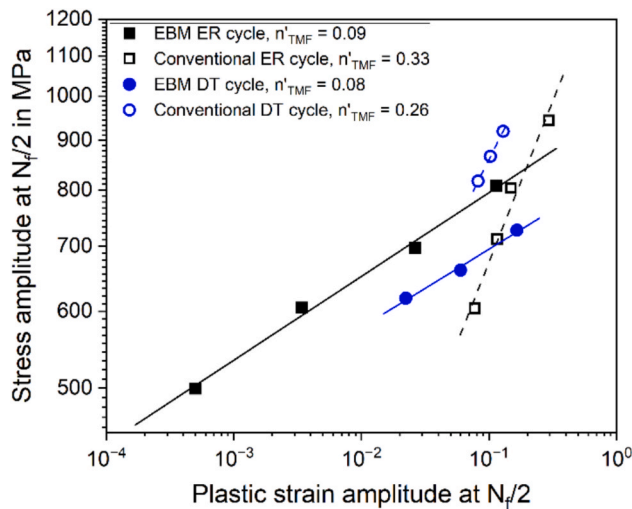


**Fig. 5.** Cyclic stress strain behaviour of conventional and EBM Inconel 718 in TMF ER and DT cycling.

strain amplitude at half of the lifetimes for all conducted TMF tests. The results confirm the indication from the hysteresis loops in Fig. 4 that introducing dwell times leads higher stress amplitudes for conventional Inconel 718, while for EBM Inconel 718, the stress amplitudes decrease. Hence, introducing dwell times causes relative hardening of conventional Inconel 718 and relative softening of EBM Inconel 718. The respective TMF hardening exponents $n'_{TMF}$, reflecting the slopes of the curves are given in the legend of Fig. 5. The values are about a factor of 3 to 4 higher for conventional material than for EBM material. Introducing dwell times barely affects the $n'_{TMF}$ values.

Fig. 6 shows the development of the stress amplitude during ER and DT cycling for EBM and conventional material at various strain amplitudes. For ER cycling, the conventional material exhibits distinct cyclic softening until failure at all tested strain amplitudes, while the EBM material shows nearly constant stress amplitudes and thus cyclically neutral behaviour. Interestingly, these tendencies are inverted for DT cycling. Here, the EBM material shows initial cyclic softening followed by a phase with nearly constant stress amplitude until failure. The conventional material exhibits initial cyclic hardening, followed by slight but continuous cyclic softening until failure.

### 3.3. Microstructural evolution

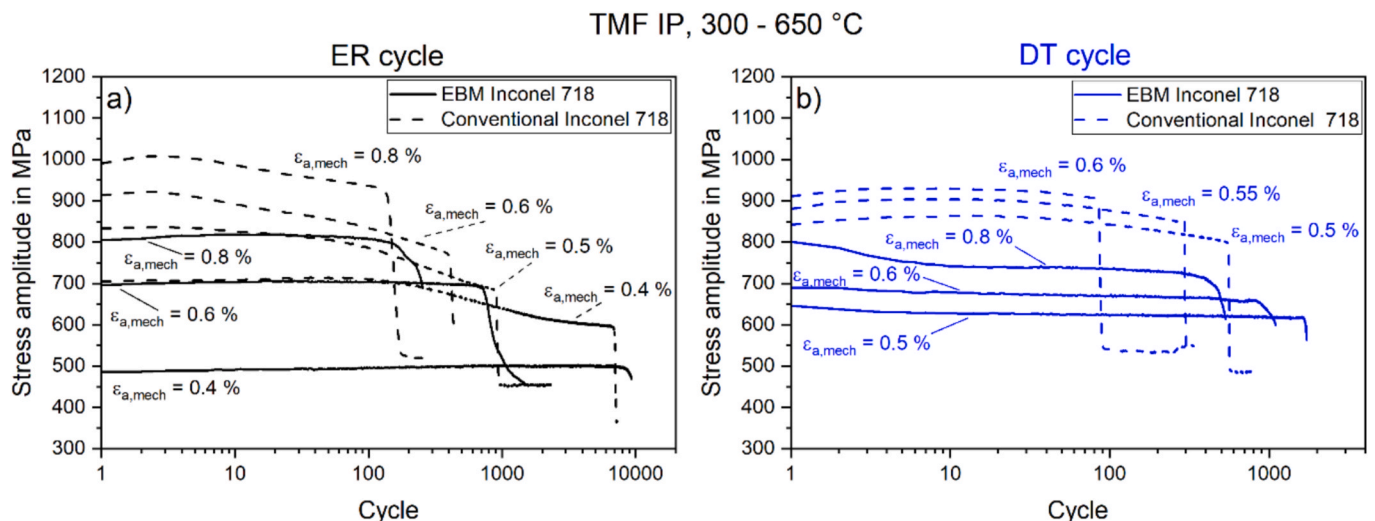Fig. 7 shows representative images illustrating the microstructural



**Fig. 6.** Influence of manufacturing method on the stress-amplitude dependent on the cycle number. a) ER cycle, b) DT cycle.
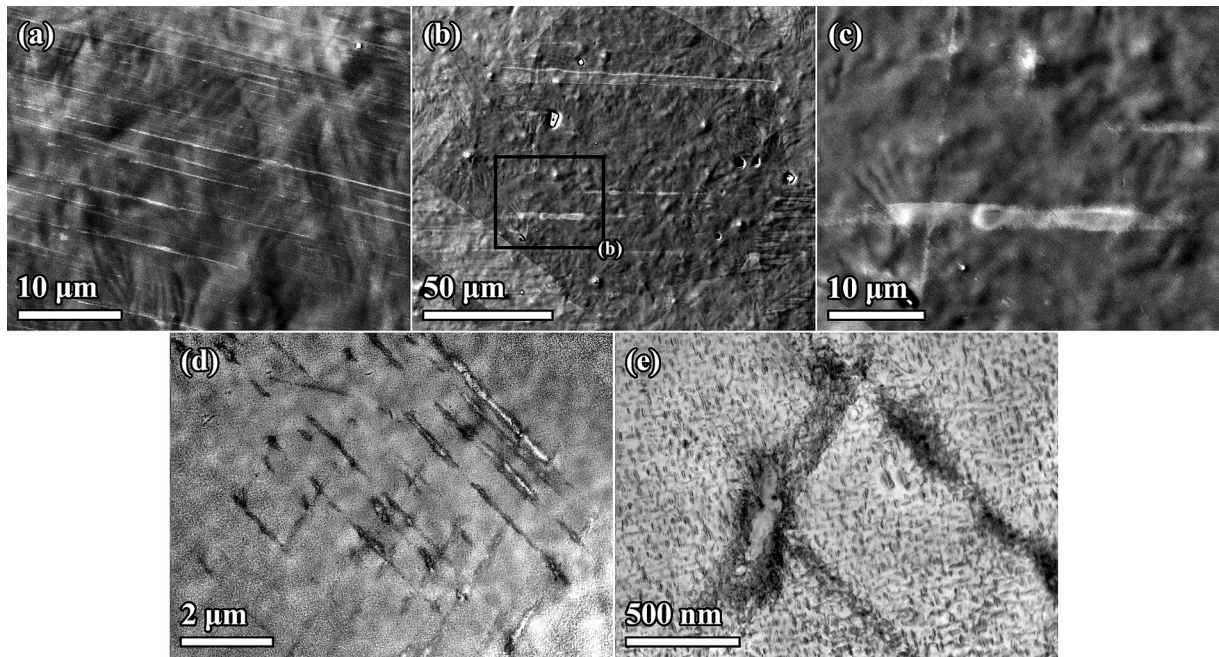
**Fig. 7.** Typical microstructures of conventional material after ER cycling. (a) – (c) ECCI micrographs after cycling with $\varepsilon_{a,mech}$ = 0.8 %, $N_f$ = 143 (a) and $\varepsilon_{a,mech}$ = 0.4 %, $N_f$ = 7001 (b and c), (d) and (e) STEM images after cycling with $\varepsilon_{a,mech}$ = 0.4 %, $N_f$ = 7001.

evolution of conventional material during ER cycling. The ECCI micrographs in Fig. 7a and 7b show pronounced planar dislocation bands running nearly parallel over large areas. The detail in Fig. 7c reveals that there are also intersecting bands indicating multiple slip systems. The STEM BF image in Fig. 7d confirms mainly planar dislocation arrangements in multiple slip systems. The detail in Fig. 7e shows that the general morphology of the γ'' precipitates is very similar to the initial state. The mean γ'' size is approximately 50 nm after both ER and DT testing, and thus remains in the same range as in the initial state. It appears that in intersecting areas of the slip bands, the γ'' precipitates have dissolved. This could be confirmed by diffraction analyses, which also showed that at the intersection of slip bands, the lattice orientation changes significantly up to 15°. For further assessment, a precipitate-free intersection area of slip bands on a TEM foil has been analysed

using TKD. The results presented in Fig. 8 show that the phase of the precipitate free area is the same as in the surrounding areas. Slight local misorientations are confirmed by the IPFZ image. The dislocation density is partly increased, which can be also seen from Fig. 7d and 7e. Fig. 9 presents the microstructure of conventional material after DT cycling. The ECCI micrograph in Fig. 9a shows similar planar dislocation bands as after ER cycling (see Fig. 6). The TEM images in Fig. 9b and 9c confirm mainly planar dislocation movement in multiple slip systems. In comparison to the microstructure after ER cycling, there are more dislocation bands, which are less pronounced, i.e., the plastic strain is less localised. The detail in Fig. 9c shows a slip band shearing several γ'' precipitates. Introducing dwell times in the TMF cycles barely affected the γ''-morphology. After DT cycling, pronounced precipitate free areas as in Fig. 7c were not observed.

For EBM material, slip bands were not observed using ECCI. Fig. 10 shows representative STEM images after ER and DT cycling with the highest applied mechanical strain amplitude of 0.8 %. While after ER cycling, some less pronounced slip bands have formed, no slip bands could be found after DT cycling. In comparison with conventional material, there is generally less dislocation content observable, which corresponds to the much lower plastic strain amplitudes for EBM material. After ER cycling, some γ''-precipitates have been sheared, while most of them remained close to their initial morphology. Some of the γ' precipitates have coarsened and were sheared by dislocations. As shown in Fig. 10c and 10d, after DT cycling, many of the γ' precipitates have coarsened preferentially in one direction, reaching lengths of up to 450 nm - more than 5 times their initial size. In the non-preferred direction, the coarsened γ' precipitates grew only by approximately 50 %. It appears that the coarsened γ' precipitates are frequently sheared by dislocations.
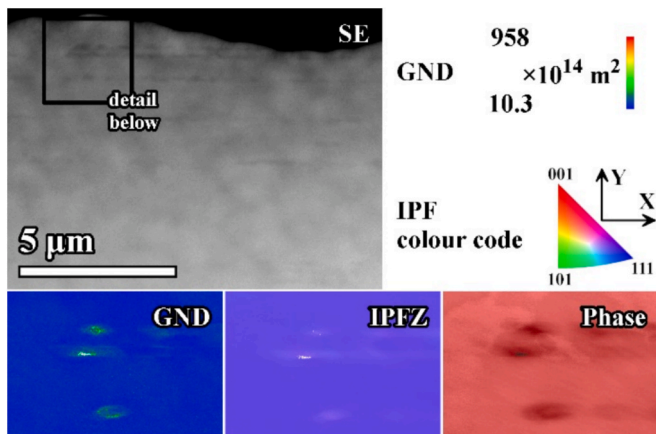
### 3.4. Damage analysis

Fig. 11 summarises the TMF damage evolution on specimens of conventional Inconel 718 after TMF ER loading. The fractographic images in Fig. 11a and 11b show facets of polygonal grains indicating that the main crack propagated mainly intergranularly. The EBSD image in Fig. 11c confirms predominantly intergranular damage on grain



**Fig. 8.** TKD analysis of a TEM foil from a conventional Inconel 718 specimen that was TMF cycled with $\varepsilon_{a,mech}$ = 0.5 %, $N_f$ = 910. The detail shows a precipitate-free area at a slip band intersection as seen in Fig. 6(e). The phase map confirms that there are no precipitates. The inverse pole figure map in z-direction (IPFZ) indicates slight orientation changes, which correspond to an increased amount of geometrically necessary dislocations (as shown in the GND map).
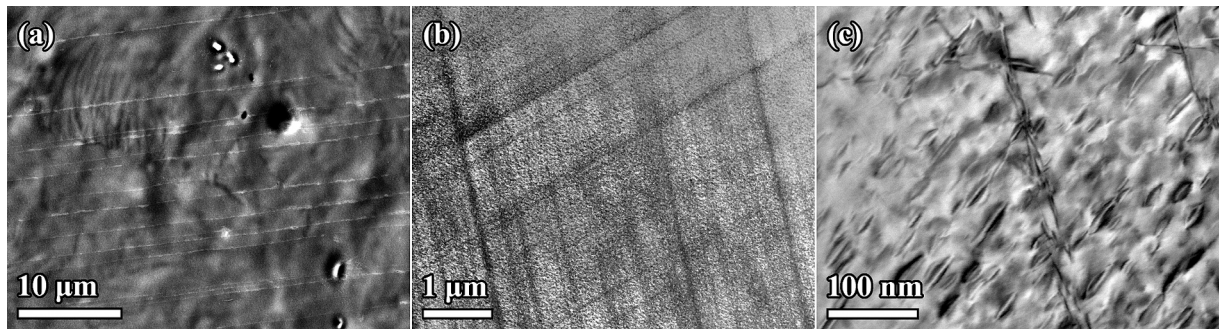
**Fig. 9.** Plastic strain localisation and microstructures of conventional material after DT cycling. (a) ECCI micrograph after TMF cycling with $\varepsilon_{a,mech}$ = 0.5 %, $N_f$ = 560, (b) and (c) TEM images after cycling with $\varepsilon_{a,mech}$ = 0.6 %, $N_f$ = 87 and $\varepsilon_{a,mech}$ = 0.5 %, $N_f$ = 560, respectively.
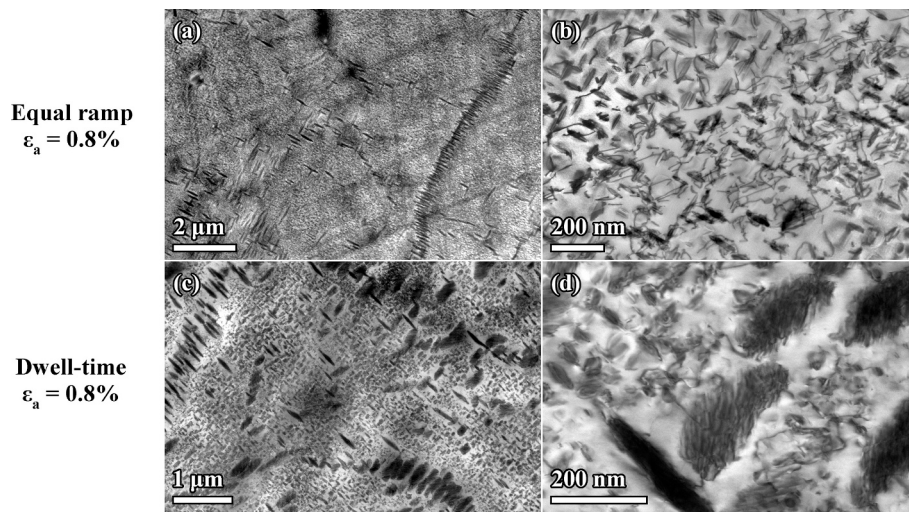


**Fig. 10.** STEM brightfield micrographs of EBM material after TMF testing. (a) and (b) ER cycling with $\varepsilon_{a,mech}$ = 0.8 %, $N_f$ = 186; (c) and (d) DT cycling with $\varepsilon_{a,mech}$ = 0.8 %, $N_f$ = 488.
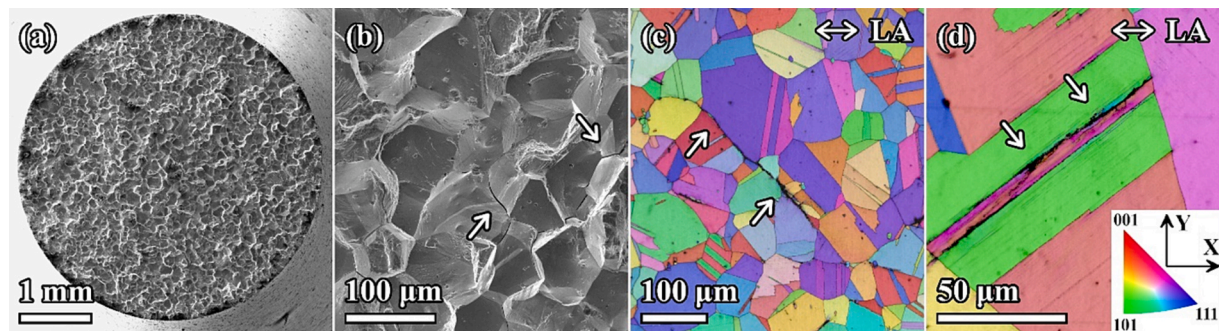


**Fig. 11.** Representative damage on failed specimens of conventional Inconel 718. (a) and (b), fracture surface with grain facets after ER cycling with $\varepsilon_{a,mech}$ = 0.4 %, $N_f$ = 7001; (c) and (d) EBSD images of longitudinal sections showing intergranular damage and cracked twin boundaries after DT cycling with $\varepsilon_{a,mech}$ = 0.5 %, $N_f$ = 560.

boundaries. Besides grain boundaries, twin boundaries were also frequently cracked, as can be seen from Fig. 11d. As expected, the amount of intergranular damage increased with the introduction of tensile dwell times in TMF DT tests.

Representative damage on EBM specimens after TMF ER loading is shown in Fig. 12. On the fracture surface in Fig. 12a, there are facets of the typical grains of the EBM material implying intergranular cracking. The detail in Fig. 12b reveals striations indicating mixed-mode transgranular and intergranular cracking. The longitudinal section in Fig. 12c shows multiple surface cracks, which initiated approximately under an

angle of 45° to the loading axis. It can be seen that the near surface area is depleted of precipitates. Further, there are needle-like precipitates in the centre of the image, which could be found in small quantities in all EBM specimens but not in conventional material. Selected area diffraction confirmed them as η phase. For the damage evolution under the testing conditions investigated in this work, the η precipitates seem to play only an insignificant role since cracking in the vicinity of such needle-shaped precipitates was not observed. Similar to conventional specimens, EBM specimens also formed frequent intergranular creep cavities during TMF-ER cycling as can be seen in Fig. 12d. Introducing
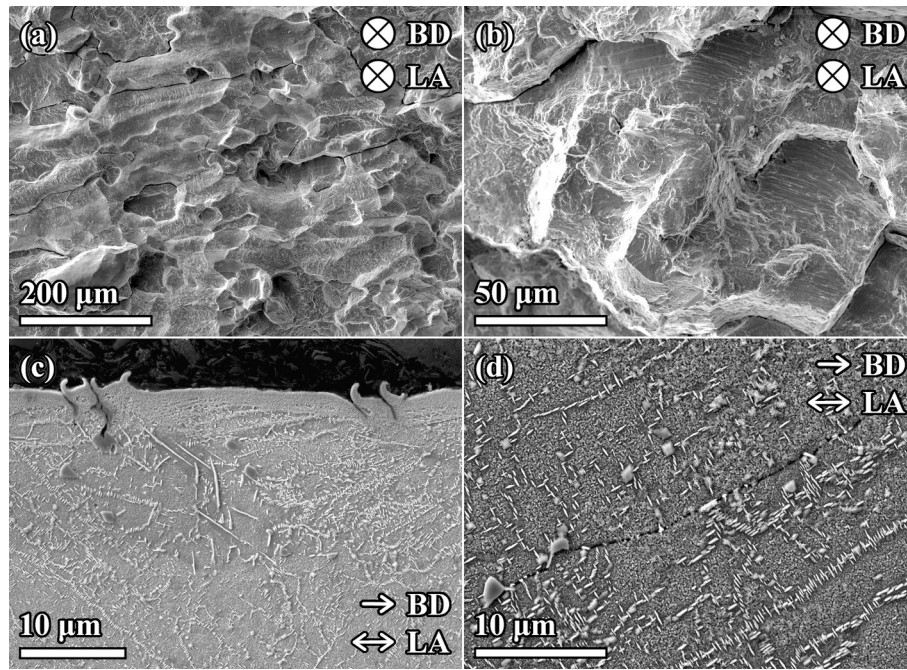
**Fig. 12.** Representative damage of failed EBM Inconel 718 specimens after TMF ER cycling. (a) and (b), fracture surface showing grain facets and striations after cycling with $\varepsilon_{a,mech}$ = 0.6 %, $N_f$ = 757 and $\varepsilon_{a,mech}$ = 0.8 %, $N_f$ = 186, respectively; (c) longitudinal section showing multiple surface crack initiations and (d) intergranular cracking on a longitudinal section, both after cycling with $\varepsilon_{a,mech}$ = 0.8 %, $N_f$ = 186.

dwell times increased the amount of intergranular damage as illustrated in Fig. 13. From the EBSD image in Fig. 13b, it can be seen that the intergranular damage concentrates in areas with fine equiaxed grains without texture.

## 4. Discussion

### 4.1. Microstructure and deformation behaviour

The results emphasise that the different initial microstructures of conventional and EBM Inconel 718 cause significant differences in the deformation behaviour under TMF loading. Most prominently, the lower elastic modulus of the EBM material due to the significant [001]-texture in loading direction leads to lower induced stresses under strain-controlled TMF testing. Since the flow stress at which plastic deformation sets in for the EBM material is not substantially lower than that of the conventional material, the EBM material also exhibits lower plastic strain amplitudes, see Fig. 4. This explains the observed much lower amount of dislocation slip bands in TMF loaded EBM material when compared to conventional material (Fig. 7 and Fig. 10) [16]. In ER tests of conventional material, the slip bands concentrate so that plastic

deformation is highly localised. This is presumably related to the more pronounced cyclic softening observed in ER tests, which is typical for Inconel 718 under TMF loading [10,20] and also under isothermal fatigue loading at 650 °C [15,17]. When slip concentrates in a few bands, the precipitates intersecting these bands will be sheared frequently up to the point that they effectively dissolve. This produces precipitate-free zones in dislocation-rich areas such as slip band intersections (Fig. 7d and 7e), which facilitate further plastic deformation and thus cyclic softening [27]. Slip band intersections experience large local plastic strain amplitudes which results in increasing misorientation (Fig. 8). Such areas may be interpreted as incipient subgrains facilitated by dynamic recovery processes due to the elevated testing temperatures. Although such effects could be frequently observed, the overall volume of these subgrains appears to be too small to have a noticeable influence on the macroscopic deformation behaviour. Coarsening of γ'' precipitates during both ER and DT cycling was not observed, which is in accordance with observations of Bartošak et al. after isothermal testing of conventional Inconel 718 [17]. Hence, we attribute the cyclic softening in ER tests of conventional material to precipitate shearing along the highly localised dislocation slip bands as proposed by Fournier and Pineau [15].
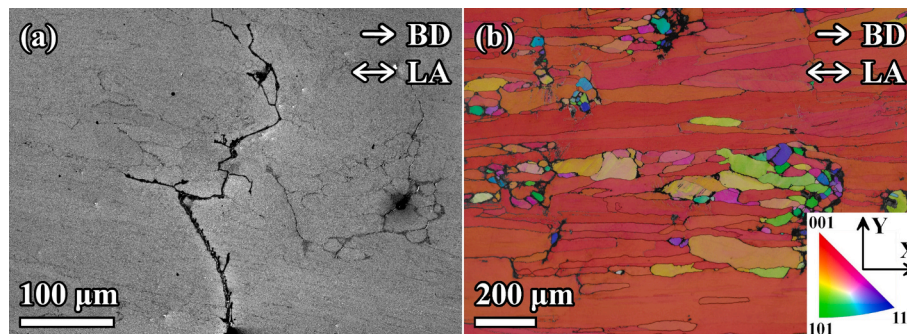


**Fig. 13.** Representative damage on a longitudinal section of a failed EBM specimen after TMF DT cycling with $\varepsilon_{a,mech}$ = 0.8 %, $N_f$ = 488. (a) intergranular crack network; (b) damage concentration in areas with fine equiaxed grains with random orientation.

After DT TMF testing of conventional material, slip bands are more evenly distributed (compare Fig. 9b and Fig. 7d) and precipitation-free zones were not observed. Apparently, dwell times promote cross slip and diffusion-mediated climbing of dislocations, which counteracts strain localisation. For a given plastic strain amplitude, it can be assumed that the slip intensity of individual slip bands decreases when the slip bands are more evenly distributed. Consequently, during DT testing of conventional Inconel 718, γ''-precipitates are less frequently sheared than in ER tests, which explains the rather neutral cyclic behaviour observed in DT tests (Fig. 6). A further effect, which may contribute to the observed higher stress amplitudes of conventional Inconel 718 due to dwell times at 650 °C, may be precipitate formation during the dwells. Slama et al. [30] found that the hardness of solution annealed Inconel 718 increased appreciably upon ageing at 650 °C and explained it with the formation of γ'-precipitates. In our case, the material is already precipitation hardened and further precipitation during TMF cycling should be rather limited. However, re-precipitation of cut and dissolved precipitates might be possible. The TEM results cannot verify this assumption since the precipitation structures after DT and ER cycling are qualitatively not discriminable. Interestingly, isothermal fatigue tests on conventional Inconel 718 with optional tensile dwells at 650 °C reported in the literature do not indicate reduced cyclic softening due to the dwells [12,17]. Bartošak et al. found nuclei of δ phase particles in slip bands after isothermal cycling with 600 s dwells, which was not observed in our case [17]. Since under TMF conditions the slip bands form mainly at temperatures below 650 °C, their structure appears to differ slightly from those formed under isothermal fatigue loading at 650 °C, eventually affecting the deformation behaviour. Revealing these differences would require a direct comparison of dislocation structures after TMF and isothermal loading. This finding highlights again the necessity of TMF testing under near-service conditions.

In comparison to conventional material, the initial precipitation structure of the EBM material appears to be mostly stable during ER testing. The much fewer slip bands in EBM material shear precipitates only occasionally resulting in a cyclically neutral behaviour. Introducing dwell times leads to significant coarsening, mainly of the γ' precipitates. This explains the observed softening of EBM material in DT tests, as reported in our previous study [26]. In comparison, conventional Inconel 718 exhibits only a minor share of γ' precipitates, which may coarsen during dwell times. Accordingly, cyclic softening effects due to sustained exposure to elevated temperatures play only a minor role for conventional material.

### 4.2. Damage and lifetime

For conventional Inconel 718, the observed damage is predominantly intergranular, which is typical for IP TMF loading [10,20,21]. The behaviour can be ascribed to tensile stresses acting at high temperatures, which produce intergranular creep cavities as well as wedge-type cracks through grain boundary sliding [7]. The grain boundaries degrade further due to oxidation at elevated temperatures [31] and offer then a preferential way for intergranular crack propagation. Introducing dwell times intensifies these mechanisms and the amount of intergranular cracking increases [11]. The observed twin boundary cracking (Fig. 11d) has been frequently found during fatigue loading of Inconel 718 and other Ni-based superalloys [14,32–34] and produces further preferential crack paths in the bulk. The EBM material shows a mixed-mode trans- and intergranular cracking, which is clearly demonstrated by the striations on the fracture surface in Fig. 12b. The initiating cracks in Fig. 12c appear also to be transgranular. Due to the columnar grain structure of the EBM material, the crack path for intergranular cracking would sometimes have a high angle to the loading direction and thus be unfavourable. In such cases, cracks may switch to transgranular growth instead. This effect may be beneficial for the TMF lifetime since under TMF IP conditions, transgranular crack propagation may be slower than intergranular crack propagation along pre-damaged grain boundaries.

However, this possible advantage of the EBM material is significantly counterbalanced by the fine equiaxed grains without texture offering a favourable intergranular crack path (Fig. 13b). The fine equiaxed grains originate presumably from aggregation of powder particles, which are not or only partially molten [35]. An optimized EBM process may provide a fully elongated grain structure, e.g. [24], which may exhibit longer IP TMF lifetimes than the material tested here. With regard to twin boundary cracking, the EBM material may be advantageous since it does not show any annealing twins even after the HIP treatment at 1120 °C. As already mentioned in our previous study, this indicates furthermore a good thermal stability of the EBM microstructure [26].

In the considered lifetime range, the stress amplitude in the midlife cycle is well suited to describe the TMF lifetimes of EBM and conventional material under both ER and DT conditions (Fig. 3b). For a given stress amplitude, lifetimes of conventional specimens are slightly longer than for EBM specimens. This implies that the conventional microstructure has a better TMF resistance than the EBM microstructure, particularly when considering that conventional material exhibits also higher plastic strain amplitudes for a given stress amplitude (Fig. 5). Consequently, the longer lifetimes for the EBM specimens are mainly a result of the low elastic modulus along the loading direction resulting in low stress amplitudes [36]. Since TMF in service is mainly strain-controlled, the EBM material may still offer potential as long as the loading is mainly uniaxial along the building direction. However, for loading perpendicular to the building direction, the IP TMF resistance of the EBM material has to be assumed as rather low [24,37].

The dependence of the lifetime on the stress amplitude contributes also to the observed influence of dwell times on the lifetime. As discussed in section 4.1, introducing dwell times increases the stress amplitude for conventional Inconel 718, which in turn reduces the lifetime since intergranular cracks grow faster. The more homogeneously distributed slip in dwell time testing of conventional material may have a positive effect on the fatigue lifetime [38]. However, since the damage concentrates on grain boundaries, possible effects of more homogeneous slip are presumably minor in comparison to grain boundary degradation due to dwell times. As opposed to conventional Inconel 718, EBM Inconel 718 cyclically softens when dwell times are introduced, which reduces stress amplitudes and the propensity of crack propagation. For high strain amplitudes, this may even lead to prolonged EBM lifetimes due to dwells (see [26] for more detailed explanation). Hence, varying effects of dwell times on the cyclic deformation behaviour of EBM and conventional material are responsible for the large lifetime differences with respect to the mechanical strain amplitude (Fig. 3a). With decreasing strain amplitude, the deformation behaviour becomes more and more elastic, and cyclic hardening and softening effects due to dwell times diminish, see Fig. 6. On the other side, for lower strain amplitudes and thus higher cycle numbers, time-dependent damage mechanisms such as grain boundary oxidation and cavity formation become increasingly dominant. Consequently, the lifetime advantage of EBM over conventional Inconel 718 in dwell time tests decreases with decreasing mechanical strain amplitude. As pointed out in our previous study, the increasing influence of time-dependent damage mechanisms at lower strain amplitudes contributes to the higher slope of the DT strain-life curve when compared to the ER strain-life curve [26]. For conventional material, it is reflected in the downward bend of the DT strain-life curve.

## 5. Conclusions

To assess the potential of additively manufactured EBM Inconel 718 for high-temperature components, comparative strain-controlled TMF tests under in-phase conditions with a temperature range of 300–650 °C and optional 600 s dwell times at 650 °C have been performed on EBM and conventionally rolled specimens. The main findings can be summarized as follows:

1. For a given mechanical strain amplitude, the EBM material exhibits longer TMF lifetimes than the conventional material. This can be mainly related to the strong [001]-texture along the building and loading direction of the EBM specimens, leading to a low elastic modulus and thus to lower induced stress amplitudes during cycling. The lifetime advantage of the EBM material is particularly pronounced in dwell time tests emphasising the potential of the EBM Inconel 718 for service in hot-operating applications.

2. The conventional Inconel 718 tends to cyclic softening due to dislocation slip bands shearing γ''-precipitates. In this regard, the EBM material is more stable, since the low elastic modulus results in low plastic strain amplitudes and therefore a significantly lower amount of slip bands. Introducing dwell times leads to coarsening of the γ' precipitates in the EBM material and thus to cyclic softening. The conventional material exhibits very few γ' precipitates, so it does not soften due to coarsening in dwell time tests. Instead, dwell times reduce the localisation of dislocations into slip bands, which reduces the effect cyclic softening.

3. For both EBM and conventional materials, in-phase TMF cycling produces intergranular damage that provides a preferential crack path. Introducing dwells intensifies intergranular damage. In conventional material, damage concentrates also at twin boundaries. Due to the columnar grain structure of the EBM material, cracks change sometimes to transgranular propagation. However, this potential benefit is significantly reduced by regions containing fine equiaxed grains, where intergranular damage concentrates. Reducing the amount of these equiaxed grains may improve the TMF resistance of the EBM material.

## CRediT authorship contribution statement

**Stefan Guth:** Writing – original draft, Supervision, Investigation, Conceptualization. **Tomaš Babinský:** Writing – review & editing, Visualization, Investigation. **Steffen Antusch:** Writing – review & editing, Resources. **Alexander Klein:** Resources. **Daniel Kuntz:** Resources. **Ivo Šulák:** Writing – review & editing, Supervision, Investigation.

## Declaration of competing interest

The authors declare that they have no known competing financial interests or personal relationships that could have appeared to influence the work reported in this paper.

## Acknowledgments

## Data availability

Data will be made available on request.

## References

[1] Sundararaman M, Mukhopadhyay P, Banerjee S. Precipitation of the δ-Ni3Nb phase in two nickel base superalloys. Metall Trans A 1988;19:453–65. https://doi.org/10.1007/BF02649259.

[2] Special Metals, INCONEL Alloy 718, Publication Number SMC-045, (2007).

[3] Hosseini E, Popovich VA. A review of mechanical properties of additively manufactured Inconel 718. Addit Manuf 2019;30:100877. https://doi.org/10.1016/j.addma.2019.100877.

[4] Körner C, Helmer H, Bauereiß A, Singer RF. Tailoring the grain structure of IN718 during selective electron beam melting. MATEC Web of Conferences 2014;14:08001. https://doi.org/10.1051/matecconf/20141408001.

[5] Popovich VA, Borisov EV, Popovich AA, Sufiiarov VS, Masaylo DV, Alzina L. Functionally graded Inconel 718 processed by additive manufacturing: Crystallographic texture, anisotropy of microstructure and mechanical properties. Mater Des 2017;114:441–9. https://doi.org/10.1016/j.matdes.2016.10.075.

[6] Šulák I, Obrtlík K. Thermomechanical and isothermal fatigue properties of MAR-M247 superalloy. Theor Appl Fract Mech 2024;131:104443. https://doi.org/10.1016/j.tafmec.2024.104443.

[7] Guth S, Lang K-H. An approach to lifetime prediction for a wrought Ni-base alloy under thermo-mechanical fatigue with various phase angles between temperature and mechanical strain. Int J Fatigue 2017;99:286–94. https://doi.org/10.1016/j.ijfatigue.2016.10.015.

[8] Zauter R, Christ HJ, Mughrabi H. Some aspects of thermomechanical fatigue of AISI 304L stainless steel: Part I. creep- fatigue damage. Metall Mater Trans A 1994;25:401–6. https://doi.org/10.1007/BF02647985.

[9] Huang ZW, Wang ZG, Zhu SJ, Yuan FH, Wang FG. Thermomechanical fatigue behavior and life prediction of a cast nickel-based superalloy. Mater Sci Eng A 2006;432:308–16. https://doi.org/10.1016/j.msea.2006.06.061.

[10] Deng W, Xu J, Hu Y, Huang Z, Jiang L. Isothermal and thermomechanical fatigue behavior of Inconel 718 superalloy. Mater Sci Eng A 2019;742:813–9. https://doi.org/10.1016/j.msea.2018.11.052.

[11] Moverare JJ, Gustafsson D. Hold-time effect on the thermo-mechanical fatigue crack growth behaviour of Inconel 718. Mater Sci Eng A 2011;528:8660–70. https://doi.org/10.1016/j.msea.2011.08.027.

[12] Barat K, Sivaprasad S, Kar SK, Tarafder S. Low-cycle fatigue of IN 718: effect of waveform. Fatigue Fract Eng Mat Struct 2019;42:2823–43. https://doi.org/10.1111/ffe.13127.

[13] Zhao J, Li B, Chen G, Itoh T, Chen X. Effects of dwell time on the isothermal and thermomechanical fatigue behavior of 316LN stainless steel. Int J Fatigue 2022;162:106989. https://doi.org/10.1016/j.ijfatigue.2022.106989.

[14] Merrick HF. The low cycle fatigue of three wrought nickel-base alloys. Metall Trans 1974;5:891–7. https://doi.org/10.1007/BF02643144.

[15] Fournier D, Pineau A. Low cycle fatigue behavior of inconel 718 at 298 K and 823 K. Metall Trans A 1977;8:1095–105. https://doi.org/10.1007/BF02667395.

[16] Worthem DW, Robertson IM, Leckie FA, Socie DF, Altstetter CJ. Inhomogeneous deformation in INCONEL 718 during monotonic and cyclic loadings. Metall Trans A 1990;21:3215–20. https://doi.org/10.1007/BF02647316.

[17] Bartošák M, Horváth J, Gálíková M, Slaný M, Šulák I. High-temperature low-cycle fatigue and fatigue–creep behaviour of Inconel 718 superalloy: damage and deformation mechanisms. Int J Fatigue 2024;186:108369. https://doi.org/10.1016/j.ijfatigue.2024.108369.

[18] Bartošák M, Mára V, Šulák I. Effects of temperature and strain rate on isothermal low-cycle fatigue behaviour of Inconel 718 superalloy: damage mechanisms, microstructure evolution, and life prediction. Int J Fatigue 2025;198:109005. https://doi.org/10.1016/j.ijfatigue.2025.109005.

[19] Kuwabara K, Nitta A, Kitamura T. Thermal-mechanical fatigue life prediction in high-temperature component materials for power plant, in. In: Proceedings of ASME International Conference on Advances in Life Prediction Methods; 1983. p. 131–41.

[20] Sun J, Yuan H. Life assessment of multiaxial thermomechanical fatigue of a nickel-based superalloy Inconel 718. Int J Fatigue 2019;120:228–40. https://doi.org/10.1016/j.ijfatigue.2018.11.018.

[21] Evans W, Screech J, Williams S. Thermo-mechanical fatigue and fracture of INCO718. Int J Fatigue 2008;30:257–67. https://doi.org/10.1016/j.ijfatigue.2007.01.041.

[22] Pollock TM, Tin S. Nickel-based superalloys for advanced turbine engines: chemistry, microstructure and properties. J Propul Power 2006;22:361–74. https://doi.org/10.2514/1.18239.

[23] Ramsperger M, Eichler S. Electron beam based additive manufacturing of alloy 247 for turbine engine application: from research towards industrialization. Metall Mater Trans A 2023;54:1730–43. https://doi.org/10.1007/s11661-022-06955-0.

[24] Kirka MM, Greeley DA, Hawkins C, Dehoff RR. Effect of anisotropy and texture on the low cycle fatigue behavior of Inconel 718 processed via electron beam melting. Int J Fatigue 2017;105:235–43. https://doi.org/10.1016/j.ijfatigue.2017.08.021.

[25] Deng D, Peng RL, Moverare J. A comparison study of the dwell-fatigue behaviours of additive and conventional IN718: the role of dislocation substructure on the cracking behaviour. Mater Sci Eng A 2020;797:140072. https://doi.org/10.1016/j.msea.2020.140072.

[26] Guth S, Babinský T, Antusch S, Klein A, Kuntz D, Šulák I. Creep–Fatigue Interaction of Inconel 718 Manufactured by Electron Beam Melting. Adv Eng Mater 2023;25:2300294. https://doi.org/10.1002/adem.202300294.

[27] Xiao L, Chen DL, Chaturvedi MC. Shearing of γ'' precipitates and formation of planar slip bands in Inconel 718 during cyclic deformation. Scr Mater 2005;52:603–7. https://doi.org/10.1016/j.scriptamat.2004.11.023.

[28] Kirka MM, Unocic KA, Raghavan N, Medina F, Dehoff RR, Babu SS. Microstructure development in electron beam-melted inconel 718 and associated tensile properties. JOM 2016;68:1012–20. https://doi.org/10.1007/s11837-016-1812-6.

[29] Kumara C, Deng D, Moverare J, Nylén P. Modelling of anisotropic elastic properties in alloy 718 built by electron beam melting. Mater Sci Technol 2018;34:529–37. https://doi.org/10.1080/02670836.2018.1426258.

[30] Slama C, Servant C, Cizeron G. Aging of the Inconel 718 alloy between 500 and 750 °C. J Mater Res 1997;12:2298–316. https://doi.org/10.1557/JMR.1997.0306.

[31] Pédron JP, Pineau A. The effect of microstructure and environment on the crack growth behaviour of Inconel 718 alloy at 650 °C under fatigue, creep and

combined loading. Mater Sci Eng 1982;56:143–56. https://doi.org/10.1016/0025-5416(82)90167-7.

[32] Stein CA, Cerrone A, Ozturk T, Lee S, Kenesei P, Tucker H, et al. Fatigue crack initiation, slip localization and twin boundaries in a nickel-based superalloy. Curr Opin Solid State Mater Sci 2014;18:244–52. https://doi.org/10.1016/j.cossms.2014.06.001.

[33] Gribbin S, Bicknell J, Jorgensen L, Tsukrov I, Knezevic M. Low cycle fatigue behavior of direct metal laser sintered Inconel alloy 718. Int J Fatigue 2016;93:156–67. https://doi.org/10.1016/j.ijfatigue.2016.08.019.

[34] Stinville JC, Lenthe WC, Miao J, Pollock TM. A combined grain scale elastic–plastic criterion for identification of fatigue crack initiation sites in a twin containing polycrystalline nickel-base superalloy. Acta Mater 2016;103:461–73. https://doi.org/10.1016/j.actamat.2015.09.050.

[35] Sun S-H, Koizumi Y, Saito T, Yamanaka K, Li Y-P, Cui Y, et al. Electron beam additive manufacturing of Inconel 718 alloy rods: Impact of build direction on microstructure and high-temperature tensile properties. Addit Manuf 2018;23:457–70. https://doi.org/10.1016/j.addma.2018.08.017.

[36] Balachandramurthi AR, Moverare J, Hansson T, Pederson R. Anisotropic fatigue properties of Alloy 718 manufactured by Electron Beam Powder Bed Fusion. Int J Fatigue 2020;141:105898. https://doi.org/10.1016/j.ijfatigue.2020.105898.

[37] Babinský T, Šulák I, Kuběna I, Man J, Weiser A, Švábenská E, et al. Thermomechanical fatigue of additively manufactured 316L stainless steel. Mater Sci Eng A 2023;869:144831. https://doi.org/10.1016/j.msea.2023.144831.

[38] Shao CW, Zhang P, Liu R, Zhang ZJ, Pang JC, Duan QQ, et al. A remarkable improvement of low-cycle fatigue resistance of high-Mn austenitic TWIP alloys with similar tensile properties: Importance of slip mode. Acta Mater 2016;118:196–212. https://doi.org/10.1016/j.actamat.2016.07.034.